JOURNAL OF GEOPHYSICAL RESEARCH: OCEANS, VOL. 118, 6578–6589, doi:10.1002/2013JC009319, 2013

# The generation and propagation of internal solitary waves in the South China Sea

Ying-Jung Chen,[1] Dong Shan Ko,[2] and Ping-Tung Shaw[1]

Received 2 August 2013; revised 8 October 2013; accepted 11 October 2013; published 5 December 2013.

[1] The internal wave field in the real-time numerical simulation at the Naval Research Laboratory is analyzed during April–May 2007, a period of intensive field observations in the northern South China Sea. Internal solitary waves are detected in the plots of the surface baroclinic velocity and depth-integrated energy flux. In each diurnal cycle, an internal wave crest with eastward surface velocity arrives at a location west of the Luzon Strait first and is followed by two internal wave troughs of westward surface velocity, in agreement with the arrival of a type-B and then a type-A internal solitary wave described in the literature. Sources of the B-wave and A-wave are consistent with the generation by eastward tidal currents on the western and eastern ridges in the Luzon Strait, respectively. During neap tide, a B-wave and an A-wave switch their daily arrival times to maintain the arrival sequence of an A-wave after a B-wave. Internal waves arriving at a mooring location at the same time each day are B-waves during the neap tide and A-waves during the first half of the spring tide. Otherwise, both A-waves and B-waves have a 1 h delay each day in their daily arrivals. Classification of the internal wave types based on generation gives a coherent pattern of internal wave propagation from the generation region to the continental margin in the South China Sea. The propagation speeds of both waves are higher than that of linear internal waves.

**Citation:** Chen, Y.-J., D. S. Ko, and P.-T. Shaw (2013), The generation and propagation of internal solitary waves in the South China Sea, *J. Geophys. Res. Oceans*, *118*, 6578–6589, doi:10.1002/2013JC009319.

## 1. Introduction

[2] Internal solitary waves (ISWs) have been frequently observed in the world oceans by satellite remote sensing [e.g., *Apel et al*., 1975; *Osborne and Burch*, 1980; *Klemas*, 2012]. The South China Sea is one of the areas where strong internal solitary waves have been found. ISW packets, consisting of a single wave front 1–6 km in width and 100–200 km in length, are observed west of 120.5°E in the deep basin of the northern South China Sea [*Zhao et al*., 2004]. The downward displacements at the wave front can exceed 150 m and the horizontal velocity can reach 2 m/s [*Ramp et al*., 2004; *Klymak et al*., 2006]. The large vertical displacements and velocities induced by ISWs may affect biological productivities, nutrient mixing [*Holligan et al*., 1985; *Moore and Lien*, 2007; *Kaartvedt et al*., 2012], sediment resuspension [*Quaresma et al*., 2007; *Pomar et al*., 2012], acoustic wave propagation [*Williams et al*., 2001], submarine navigation, coastal engineering, and oil exploration. Baroclinic tides moving onto the continental shelf may be the essential factor of energy for diapycnal mixing away from the surface mixed layer and the seafloor boundary layer [*Finnigan et al*., 2002].

[3] Extensive observations conducted in the last decade have provided much information on the properties of internal solitary waves in the South China Sea. Mooring and remote sensing observations have suggested that waves are generated in the Luzon Strait and propagate westward across the deep basin of the northern South China Sea [e.g., *Ramp et al*., 2004; *Zheng et al*., 2007]. Using mooring observations in the continental margin, *Ramp et al*. [2004] gave the first comprehensive description of the internal solitary waves in the northern South China Sea. Waves are generated around the time of the spring tides. Two types of waves have been observed. B-waves are weaker and have a 1 h delay in arrival each day. A-waves have greater amplitude than B-waves and arrive at a particular mooring site at the same time each day. Later with 10 moorings spanning from the Luzon Strait to the upper continental slope, *Alford et al*. [2010] studied the arrival time, speed, amplitude, width, energy, and number of trailing waves of the wave fronts. Waves begin as broad internal tides close to the ridges in the Luzon Strait and steepen in the deep basin to become solitary waves. Their widths narrow from the order of 10 km in the deep basin to the order of 100 m on the upper continental slope. In the deep basin, both A- and

[1]Department of Marine, Earth and Atmospheric Sciences, North Carolina State University, Raleigh, North Carolina, USA.
[2]Oceanography Division, Naval Research Laboratory, Stennis Space Center, Mississippi, USA.

Corresponding author: P.-T. Shaw, Department of Marine, Earth and Atmospheric Sciences, North Carolina State University, Raleigh, NC 27695-8208, USA. (pt_shaw@ncsu.edu)


2169-9275/13/10.1002/2013JC009319

B-waves propagate faster than the phase speed of linear waves. However, B-waves propagate faster than A-waves on the continental slope. *Alford et al*. [2010] confirmed the findings of *Ramp et al*. [2004] that waves appear twice daily in a particular pattern of narrower A-waves alternating with wider, smaller B-waves. They further noted that A-waves follow B-waves more closely than in the reverse order.

[4] Figure 1 shows the submarine topography in the northern South China Sea. Two ridges are present in the Luzon Strait. The "eastern ridge" is located near 122°E, while the "western ridge" extends southward from the southern tip of Taiwan along 121°E. Observations generally suggest that internal waves are generated at these two ridges [*Ramp et al*., 2004, *Zhao and Alford*, 2006; *Alford et al*., 2011]. *Zhao and Alford* [2006] assumed that a B-wave and A-wave pair observed at a mooring site near the Dongsha Reef (117.3°E) is generated 57.6 h earlier in the Luzon Strait by two consecutive westward tidal peaks. The corresponding speed of wave propagation is 2.3 m/s. *Alford et al*. [2010] later found that the arrival times of ISWs at moorings in the deep basin are 6–8 h later than predicted by *Zhao and Alford* [2006] and suspected that ISWs are generated at the eastern ridge shortly after eastward tidal currents. However, *Alford et al*. [2010] could not reconcile the short lag time of an A-wave behind a B-wave.

[5] There are two reasons why the specific ridges and the phase of tides at generation are not determined by observations. First, nonlinear internal waves are not seen in satellite imagery east of about 120.5°E [e.g., *Zhao et al*., 2004], making it not possible to extrapolate waves to the generation site. Second, the phase relationship between the tidal currents and the internal waves is not resolved by moorings near the generation site because of the strong flow, insufficient vertical depth coverage, and contamination of westward energy flux by eastward propagating waves generated at the western ridge [*Alford et al*., 2010].

[6] Another unresolved issue is the mechanism of wave generation in the Luzon Strait. *Lien et al*. [2005] favored the internal tide mechanism of *Lee and Beardsley* [1974] over the lee-wave mechanism of *Maxworthy* [1979] for ISW generation. They argued that lee waves are not observed near the ridges in the Luzon Strait. *Zhao and Alford* [2006] also suggested the internal tide mechanism because they associated the observed A- and B-waves with the two peaks in westward tidal currents. A number of numerical simulation studies have addressed this issue. *Chao et al*. [2007] showed that internal tides are generated on the eastern ridge by the semidiurnal tides and damped by the lower western ridge. *Shaw et al*. [2009] demonstrated that ISWs originate from lee waves in the form of wave beams at a critical ridge in a two-dimensional nonhydrostatic numerical study. *Buijsman et al*. [2010] showed that an elevation wave west of the eastern ridge instead of a lee wave is created by the eastward tidal current and westward propagating solitons form on the back slope of the elevation wave. Using a three-dimensional nonhydrostatic model, *Zhang et al*. [2011] suggested that A- and B-waves arise from steepening of internal tides from the eastern ridge in the Luzon Strait, lining up with peak eastward and westward semidiurnal barotropic currents, respectively. *Vlasenko et al*. [2012] reproduced the observed A- and B-waves in *Alford et al*. [2010] in a two-dimensional nonhydrostatic simulation using a bottom profile averaged between 20.25°N and 20.75°N. They also noted a permanent transition between the two wave types.

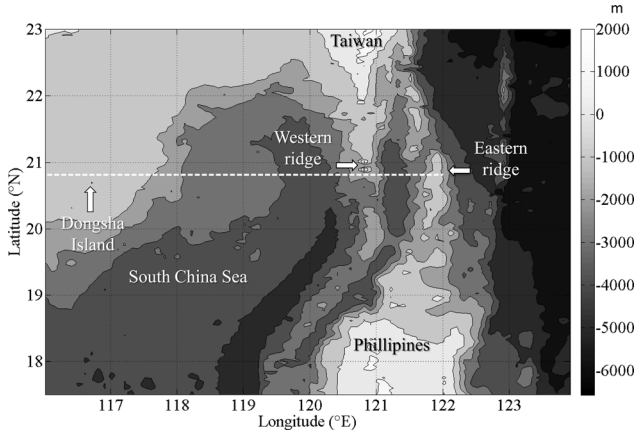


**Figure 1.** Map of the northern South China Sea showing the locations of the Dongsha Island and two ridges in the Luzon Strait. The latitude 20.81°N is along the dashed line. The depth contour is in meters with a contour interval of 1000 m.

[7] Multiple tidal constituents are often included in the numerical studies. However, many earlier studies are two-dimensional. The complex bottom topography in the Luzon Strait, the region of internal wave generation, is not adequately represented. In addition, all studies except *Chao et al*. [2007] use a single density profile from the South China Sea for the entire study domain. Mesoscale processes such as the Kuroshio and eddies are not simulated in real time, preventing a direct comparison with wave propagation in mooring data. In this study, data from the real-time simulation of the Naval Research Laboratory (NRL) hydrostatic basin-scale model are used to study the generation and propagation of internal waves in the northern South China Sea. The model includes realistic tidal forcing and mesoscale features such as the Kuroshio and eddies. Although the model is hydrostatic, the location of the internal wave front is well resolved in the data. Because the simulation is in real time, internal waves obtained from simulation and mooring observations can be directly compared. Ideally, a nonhydrostatic model is required to resolve the steep front of internal solitary waves. However, the small grid size of a nonhydrostatic model makes it difficult to include both the realistic tidal forcing and the mesoscale processes in the model.

[8] The organization of this paper is as follows. In section 2, data from the numerical simulation are described. The arrival time at different longitudes is analyzed for A- and B-waves in section 3. Discussions of the wave generation process and properties of each wave type are given in section 4, followed by conclusions in section 5.

## 2. Data and Methods

[9] Data used in this study are obtained from the real-time numerical simulation of the Luzon Strait Ocean Nowcast/Forecast System (LZSNFS), which is an application of

the NRL Ocean Nowcast/Forecast System [*Ko et al*., 2008] intended for short-term (under a week) ocean forecast. The system is an integration of a dynamical ocean model and a statistical data-analysis model. The ocean model is adopted from the Princeton Ocean Model with modifications to accommodate data assimilation, hybrid vertical coordinates, and multiple nesting. The statistical model produces three-dimensional ocean temperature and salinity analyses from satellite altimetry and sea surface temperature (SST) based on historical observations. For nowcast, the LZSNFS continuously modifies model temperature and salinity toward the analyses using a vertical weighting function. The analyses from satellite altimetry and SST are of low frequency, and a scale separation method is applied in the data assimilation to prevent attenuation of the high-frequency internal wave energy. Details of the numerical method are described in *Ko et al*. [2008].

[10] The LZSNFS domain covers the northern South China Sea, the Luzon Strait and a portion of the western Pacific with horizontal resolution of 2.3 km (Figure 1). For vertical resolution, there are 11 terrain-following sigma-layers in the top 147 m and 29 fixed-depth layers below with closely spaced layers in the upper water column to better resolve the upper ocean variations. The model derives its ocean bottom topography from the Digital Bathymetry Data base in 2 min resolution. Open boundary conditions are derived from a larger scale model for the entire East Asian seas [*Ko et al*., 2009]. The barotropic tidal currents of eight tidal constituents ($K_1$, $O_1$, $P_1$, $Q_1$, $K_2$, $M_2$, $N_2$, and $S_2$) are obtained from the Oregon State University Tidal Prediction Software [*Egbert and Erofeeva*, 2002]. Surface forcing of wind stress and surface atmospheric pressure is obtained from the regional Coupled Ocean/Atmosphere Mesoscale Prediction System (COAMPS) to take advantage of its high resolution. However, heat flux and solar radiation are derived from the global Navy Operational Global Atmospheric Prediction System (NOGAPS) because the heat fluxes from COAMPS, in particular in the earlier years, are judged to be poorer than those from NOGAPS. Data generated by nowcast runs have been used in several internal wave studies in the northern South China Sea [e.g., *Chao et al*., 2007; *Qian et al*., 2010].

[11] Analysis of the internal wave field in this paper is carried out along 20.81°N indicated by a dashed line in Figure 1. Data in April and May 2007 are used. The location and time are chosen to cover the intensive in situ mooring observation of *Alford et al*. [2010] and wave generation by the two ridges in the Luzon Strait. A cross-sectional view of the bottom topography along this section is shown in Figure 2. The tall eastern ridge at 121.8°E reaches the surface at this latitude. The western ridge, which is 1200 m below surface at 120.8°E, is lower and has a wider plateau than the eastern ridge. The slope is steeper on the east side than on the west side. The two ridges are separated by a trough more than 3000 m deep. The deep basin west of the western ridge is 2500–3500 m deep. Between 118.5°E and 117°E is the continental slope, where water depth decreases rapidly from 2500 to 360 m on the plateau around the Dongsha Island. Figure 2 also shows the mean temperature in April–May 2007 along 20.81°N. The upper thermocline is shallow in the deep basin of the South China Sea. The Kuroshio is located at the sloping thermocline near the western ridge.

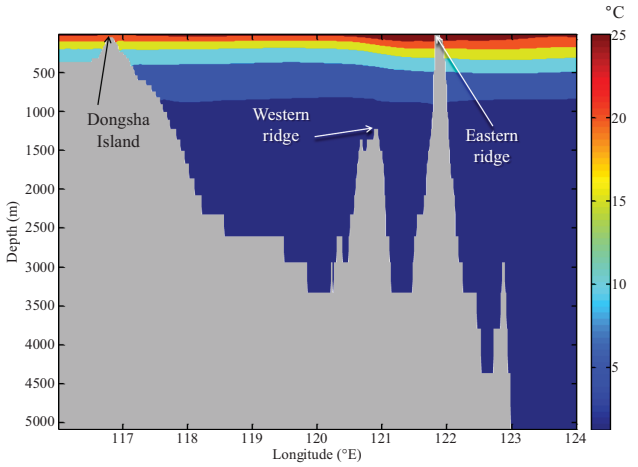


**Figure 2.** Bottom topography along 20.81°N in NRL model simulation. Contour lines show the mean temperature in °C during the study period.

[12] For internal wave analysis in this study, hourly values of temperature, salinity, and zonal velocity between 116°E and 122°E are extracted from the data archive along 20.81°N. Time series of density are first constructed from temperature and salinity using a nonlinear equation of state. For the mean field, time series of density and eastward velocity are low-pass filtered at a cutoff period of 32 h using a least-square filter with a 121-point Lanczos window [*Bloomfield*, 2000]. The cutoff period is chosen to separate the diurnal and semidiurnal internal waves from mesoscale features such as the Kuroshio.

[13] High-pass filtered time series of eastward velocity ($u$) and density ($\rho$), obtained by subtracting the mean field from the original series, represent motion caused by internal waves and tides. The eastward barotropic tidal velocity is calculated by depth averaging the velocity $u$. The barotropic velocity is then subtracted from $u$ to obtain the baroclinic velocity $u'$ representing the velocity of the internal wave. Calculation of the hydrostatic pressure in the water column follows the procedure outlined by *Qian et al*. [2010]. First, the hydrostatic pressure $p(x,z,t) = \int_z^0 \rho(x,z',t)g\mathrm{d}z'$ is obtained from the high-pass filtered density time series by integration from vertical coordinate $z$ to the surface. Following *Nash et al*. [2005], the depth averaged pressure is subtracted to obtain the perturbation pressure $p'(x,z,t) = p(x,z,t) - \int_{-H}^0 p(x,z',t)\mathrm{d}z'/H$, where $H$ is the bottom depth. The depth-integrated eastward energy flux over the whole water column $\int_{-H}^0 u'p'\mathrm{d}z$ is then calculated and used to track internal waves in this study.

## 3. Result

### 3.1. Wave Arrival Pattern and Generation

[14] In this section, the zonal component of the tidal velocity, baroclinic velocity at 62.5 m, and depth-integrated energy flux is used to demonstrate the wave pattern at 119.5°E, the longitude where both A-waves and B-waves can be identified closest to the Luzon Strait. Figure 3

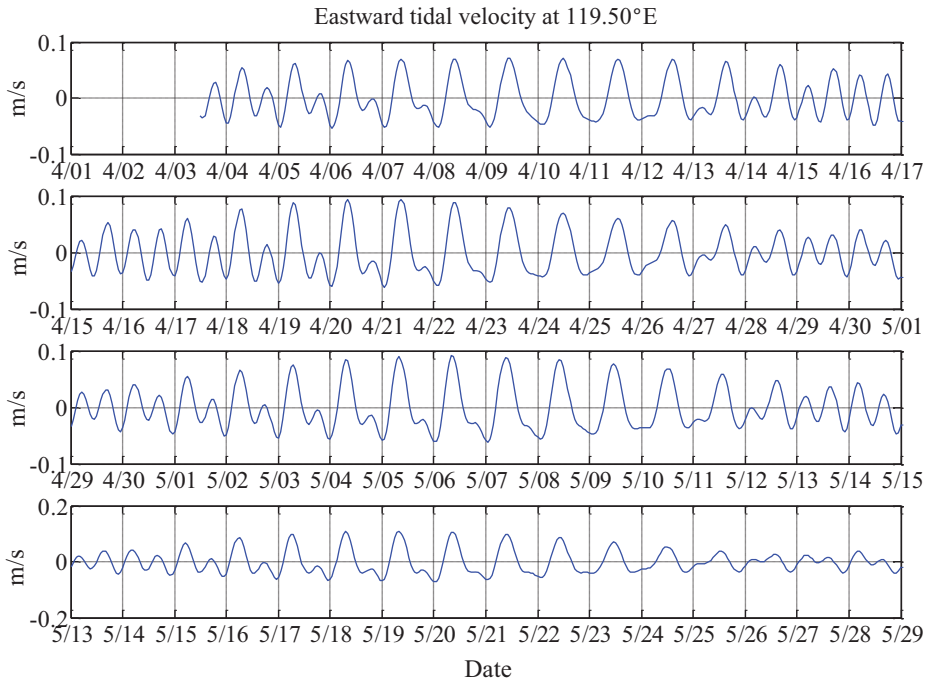


**Figure 3.** Time series of the eastward tidal velocity at 20.81°N, 119.5°E in April and May 2007. Each panel lags the previous one by a fortnightly period of 14 days. The 2 day overlapping in adjacent panels shows the repetition of the spring-neap tide cycle. Note that a different velocity scale is used in the last panel. Missing values at the beginning and end are due to filtering.

shows time series of the eastward tidal velocity. At a phase speed of 700 km/h and a sampling interval of 1 h, the barotropic tides in Figure 3 are representative of the tidal phase along the entire 600 km study section. In each panel, the spring tide occurs in the middle, and the neap tide is at the beginning and end. A semidiurnal component appears at the beginning of the neap tide and persists to the peak spring tide. In each panel, the two semidiurnal peaks are about equal at the end of the first day. After day 2, the second semidiurnal peak of the day decreases in size while the first one grows quickly to become a large diurnal peak. Note that the eastward and westward tidal currents are not symmetric during the diurnal tide; peaks of the eastward tidal currents are larger and narrower than those of westward tidal currents. Tides return to semidiurnal at the end of each panel. The oscillation is nearly sinusoidal during the neap tide.

[15] Figure 4 shows time series of the baroclinic velocity ($u'$) at 62.5 m and 119.5°E. The pattern follows the spring-neap cycle closely, consisting of wave crests of positive velocity and wave troughs of negative velocity. However, the wave crest and trough are not symmetrical: crests are more rounded while troughs tend to form a pointed end. Furthermore, a particular sequence of wave crests and troughs can be identified. For example, a broad crest in the latter half of 6 April is followed by two wave troughs on 7 April with little positive flow between the two troughs. The first trough forms a sharp, pointed negative peak. It is well known that nonlinear internal solitary waves in the northern South China Sea form at the leading edge of a wave trough of westward surface velocity [e.g., *Ramp et al*., 2004; *Shaw et al*., 2009]. A pointed negative peak in Figure 4 thus indicates the location of a wave front. The peak may be stronger in the first trough behind a crest (7 April) or in the second trough (18 May). A third trough may develop occasionally (17 May). This pattern repeats in the next 6 days until the two troughs merge to one on 11–12 April. Soon afterward, the trough intensifies on the back side and a new trough tends to develop in front of it (13–17 April). The crest-trough-trough sequence reappears at the beginning of the spring tide in the next fortnightly cycle. In the mooring data, the crest-trough-trough pattern in the baroclinic velocity is often observed [e.g., *Ramp et al*., 2004; *Alford et al*., 2010]. *Ramp et al*. [2004] refer to the first and second troughs as B- and A-waves, respectively.

[16] During the same period, the corresponding energy flux integrated over the entire water column is shown in Figure 5. A large negative peak in energy flux, indicating westward wave propagation, is often associated with a crest or a trough in Figure 4. In particular, a peak in energy flux associated with a wave trough is more likely to be sharper than one with the wave crest. Thus, an ISW is identified in this paper by a negative peak in both the depth-integrated energy flux and the surface baroclinic velocity. Figure 5 shows that ISWs are strongest at the beginning of the spring tide when the semidiurnal tides diminish. For example, the baroclinic velocity at 119.5°E (Figure 4) is positive in a wave crest at 20:00 UTC on 6 April and negative in two wave troughs at 0:00 and 10:00 on 7 April. In the plot of energy flux (Figure 5), three negative peaks correspond well with the crest and troughs, indicating the arrivals of

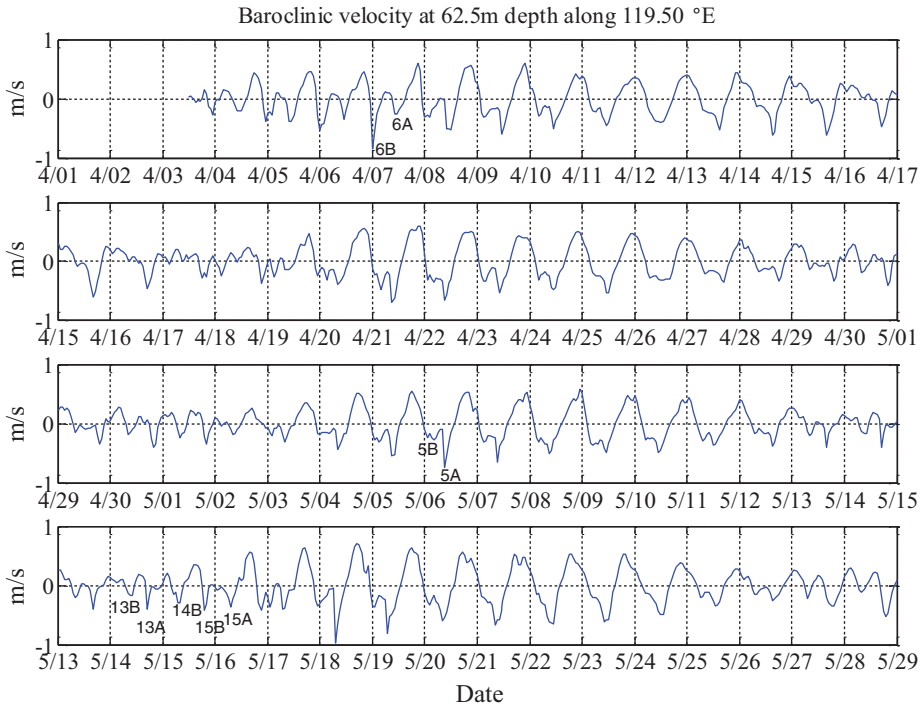


**Figure 4.** Same as in Figure 3 except for the baroclinic velocity at 62.5 m. The wave label is explained at the end of section 3.1.

positive surface flow, a strong B-wave and then an A-wave according to the definition of *Ramp et al*. [2004]. A few A- and B-waves are labeled in Figures 4 and 5. The number in the label will be explained later in this section.

[17] At a propagation speed between 2 m/s and 3 m/s [e.g., *Zhao and Alford*, 2006; *Alford et al*., 2010], the arrival time of a wave at 119.5°E will be 22–33 h after generation at the eastern ridge (121.8°E). If the B-wave at

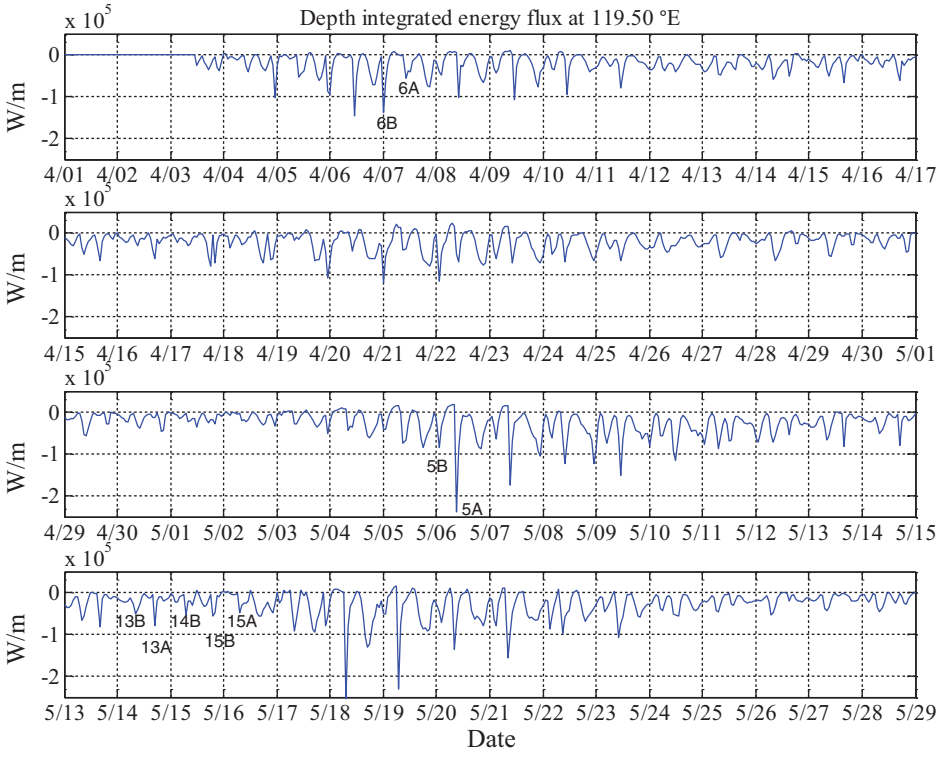


**Figure 5.** Same as in Figure 3 except for the depth-integrated energy flux over the entire water column.

**Table 1.** Wave Propagation Speeds Calculated From Arrivals of the First Cluster of ISWs at 119.5°E in Early April 2007 Based on Two Wave Generation Scenarios (See Text)[a]

| Waves at 119.5° | | | | Scenario 1 | | | Scenario 2 | | |
|---|---|---|---|---|---|---|---|---|---|
| Date | Phase | Hour | Label | Hour | Direction | Speed (m/s) | Hour | Ridge | Speed (m/s) |
| 5 April | T | 95 | 4B | | | | 79 | W | 2.5 |
| 5 April | T | 106 | 4A | 73 | Flood | 2.0 | 79 | E | 2.5 |
| 5 April | C | 115 | | 79 | Ebb | 1.8 | | | |
| 6 April | T | 120 | 5B | 85 | Flood | 1.9 | 104 | W | 2.5 |
| 6 April | T | 131 | 5A | 97 | Flood | 2.0 | 104 | E | 2.5 |
| 6 April | C | 140 | | 104 | Ebb | 1.8 | | | |
| 7 April | T | 144 | 6B | 110 | Flood | 2.0 | 128 | W | 2.5 |
| 7 April | T | 154 | 6A | 121 | Flood | 2.0 | 128 | E | 2.6 |
| 7 April | C | 165 | | 128 | Ebb | 1.8 | | | |
| 8 April | T | 170 | 7B | 135 | Flood | 1.9 | 153 | W | 2.4 |
| 8 April | T | 178 | 7A | 145 | Flood | 2.0 | 153 | E | 2.7 |
| 8 April | C | 189 | | 153 | Ebb | 1.8 | | | |
| 9 April | T | 195 | 8B | 160 | Flood | 1.9 | 178 | W | 2.4 |
| 9 April | T | 203 | 8A | 170 | Flood | 2.0 | 178 | E | 2.7 |
| 9 April | C | 214 | | 178 | Ebb | 1.8 | | | |
| 10 April | T | 220 | 9B | | | | 203 | W | 2.4 |
| 10 April | T | 227 | 9A | 194 | Flood | 2.0 | 203 | E | 2.8 |
| 10 April | C | 237 | | 203 | Ebb | 2.0 | | | |
| 11 April | T | 246 | 10B | | | | 228 | W | 2.2 |
| 11 April | T | 251 | 10A | 218 | Flood | 2.0 | 228 | E | 2.9 |

[a]The first four columns give the arrival date, wave phase (T for trough and C for crest), hour (from 0:00 UTC on 1 April 2007), and the wave label. The next two sections show the tidal phase (flood or ebb) for scenario 1 and generation site (W, western ridge; E, eastern ridge) for scenario 2.

0:00 h on 7 April (wave 6B in Figure 4) originates at the eastern ridge, its generation will be between 15:00 h on 5 April and 2:00 h on 6 April. In Figure 3, a weak maximum in the westward tidal current (flood) occurs at 14:00 h on 5 April, followed by a larger maximum in the westward tidal current at 1:00 h on 6 April, and an even larger peak in the eastward tidal velocity (ebb) at 8:00 h on 6 April. If wave 6B was generated by the stronger second peak of the flood tide, a crest of positive surface baroclinic velocity, produced by the ebb tide at 8:00 h on 6 April, would follow the B-wave. On the other hand, Figure 4 shows that an A-wave (wave 6A) is behind the B-wave with a time lag of 10 h. The wave arrival sequence is violated. If generated by the weaker first peak of the flood tide, wave 6B would be behind a crest of positive surface velocity generated by the previous ebb tide and ahead of an A-wave (6A) generated by the second peak of the flood tide, a scenario of wave generation suggested by *Zhao and Alford* [2006]. However, this scenario cannot explain why wave 6B, which is larger and narrower than wave 6A, is produced by the smaller peak in the flood tide.

[18] Another scenario that matches the time of wave arrival is to assume that the A-wave at 10:00 h on 7 April (wave 6A) is generated at the eastern ridge. In this case, wave generation occurs between 1:00 h and 12:00 h on 6 April. In Figure 3, the largest peak in the tidal cycle at 8:00 h on 6 April matches the generation time correctly. This peak is associated with the ebb tide of eastward tidal currents. Wave generation by eastward tidal currents in the Luzon Strait has been suggested by *Alford et al*. [2010] and *Buijsman et al*. [2010]. Specifically, an A-wave is released after the tidal current turns westward [*Buijsman et al*., 2010]. If the B-wave that arrives 10 h earlier (6B) also started at the eastern ridge, it would be generated by the flood tide and separated from the A-wave by a crest of positive surface velocity generated during the ebb tide. Therefore, the eastern ridge is not the source of wave 6B. A plausible source for the B-wave is the western ridge (120.9°E). In the speed range between 2 m/s and 3 m/s, wave 6B would be generated 14–20 h earlier between 4:00 and 10:00 on 6 April. The timing matches well with the peak ebb tide at 8:00 h. Thus, arrivals of the two waves are best described by wave generation at two different ridges by the same peak in the eastward tidal current.

[19] According to the above two wave generation scenarios, the wave propagation speed calculated from the first cluster of ISWs at 119.5°E in early April 2007 is shown in Table 1. A B-wave and an A-wave are generated at the eastern ridge by the two peaks in the flood tide in scenario 1 [*Zhao and Alford*, 2006]. In scenario 2, a B-wave and an A-wave are generated by the ebb tide at the western and eastern ridges, respectively. The speed of wave propagation is calculated from the distance between 119.5°E and the ridge divided by the time difference between wave arrival and generation. The first four columns give the arriving date, tidal phase (T for trough and C for crest), hour (from 0:00 UTC on 1 April 2007), and a wave label to be described later. The hour and phase of the peak ebb and flood tide are included for scenario 1. The hour of the peak ebb tide and the ridge of wave generation (E for eastern and W for western) are shown for scenario 2. The speed for scenario 1 is between 1.8 m/s and 2.0 m/s, much lower than the observed 3 m/s at 120.5°E by *Alford et al*. [2010]. The speed for scenario 2 is 2.4–2.9 m/s, closer to the observed value than scenario 1. In section 3.5, the speed for scenario 2 will be shown to match the speed of wave propagation in the data. It is concluded that scenario 2 is most likely the process of internal wave generation in the Luzon Strait.

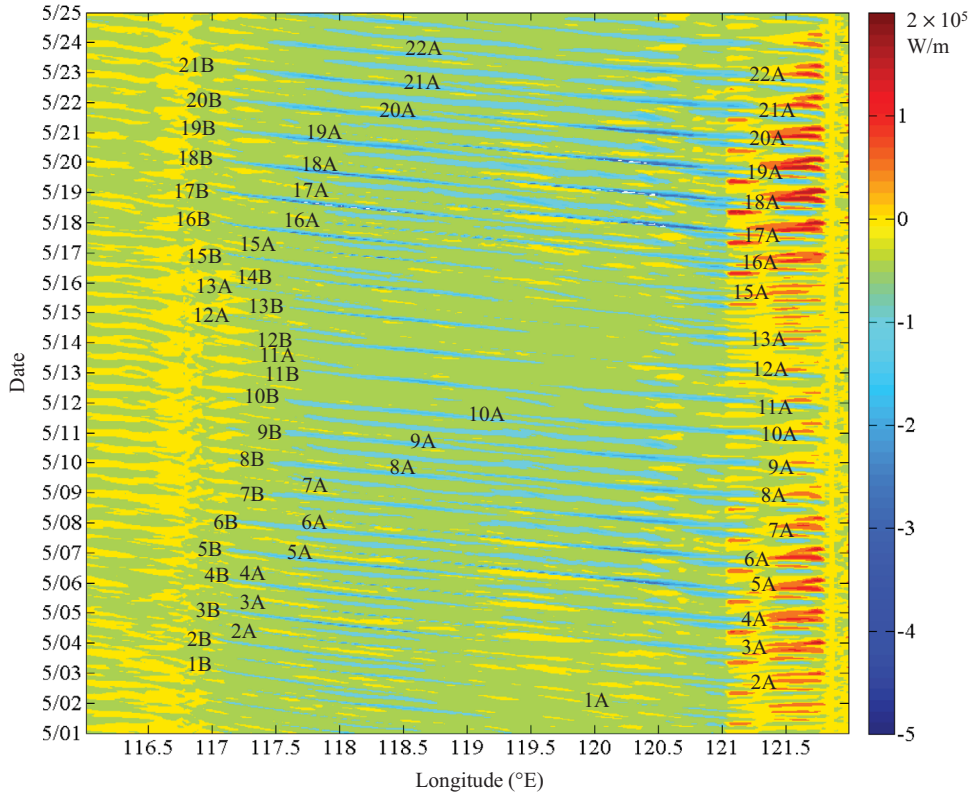


**Figure 6.** Contour plot of depth-integrated energy flux on longitude-time axes. The blue (red) color shows westward (eastward) propagating crests and troughs of internal waves. Small patches of extreme values are due to sampling at 1 day interval. Westward propagating wave troughs are labeled by the date of generation and wave type. The contour interval is $5 \times 10^4$ W/m.

Under this scenario, a maximum in the eastward tidal velocity during ebb tides generates an A-wave on the eastern ridge and a B-wave on the western ridge, producing a wave arrival sequence of a crest, a B-wave trough, and an A-wave trough in the northern South China Sea.

[20] A wave labeling scheme based on scenario 2 is used in this paper. Each wave trough in Figure 4 is labeled by its date of generation followed by a letter A or B for its type. Two troughs following a crest are generated by the same peak in the ebb tide, so both have the same number. For example, the troughs at 0:00 h and 10:00 h on 7 April are generated by tides on 6 April and are labeled as 6B and 6A, respectively.

### 3.2. Depth-Integrated Zonal Energy Flux

[21] It is well known that the internal wave propagates along slanted paths at generation and evolves into vertical normal modes [e.g., *Shaw et al.*, 2009]. Wave troughs and crests are well defined in vertical normal modes and can be identified as peaks in plots of the depth-integrated energy flux and baroclinic velocity. A contour plot of depth-integrated energy flux between 1 and 25 May 2007 is shown in Figure 6. Local minima and maxima in energy flux indicate westward and eastward wave propagation, respectively. Divergence in energy flux occurs at 121.8°E on the west slope of the eastern ridge and at 121°E on the east slope of the western ridge. Between the two ridges, both westward and eastward energy fluxes are present. Waves in Figure 6 are labeled according to the scheme given in section 3.1. Local minima are first selected and classified as a crest or a trough according to the sign of the baroclinic surface velocity (not shown). Next, the sequence of wave arrival (a wave crest, a B-wave, and an A-wave) is identified in each diurnal cycle. Each A-wave or B-wave is then traced to the peak eastward tidal velocity as described in section 3.1 to determine the date of wave generation. A lag time of 24–25 h is required for consecutive waves of the same type except when there are two semidiurnal peaks in the eastward tidal velocity (Figure 3).

[22] In Figure 6, westward energy flux of A-waves begins at about 121.2°E east of the western ridge, indicating that the western ridge is not the source of A-waves. Stronger A-waves are 1A–7A and 15A–18A, which are produced in the first half of the spring tide (Figure 3). During the neap tide, waves 11A–13A are weaker. Westward propagating A-waves can reach 117.5°E. All A-waves can be traced to a peak in the eastward barotropic tide on the west side of the eastern ridge following scenario 2 in Table 1. Westward energy flux for B-waves is present mostly between 117°E and 119.5°E. The divergence in energy flux at 121°E is consistent with the generation of B-waves at the western ridge. The generation location is further verified using scenario 2 in Table 1.

[23] All consecutive A-waves in Figure 6 have a lag time of 24–26 h, and so do all B-waves except during neap tide on May 13–14 (Figure 3). From Figure 4, wave 13A leads

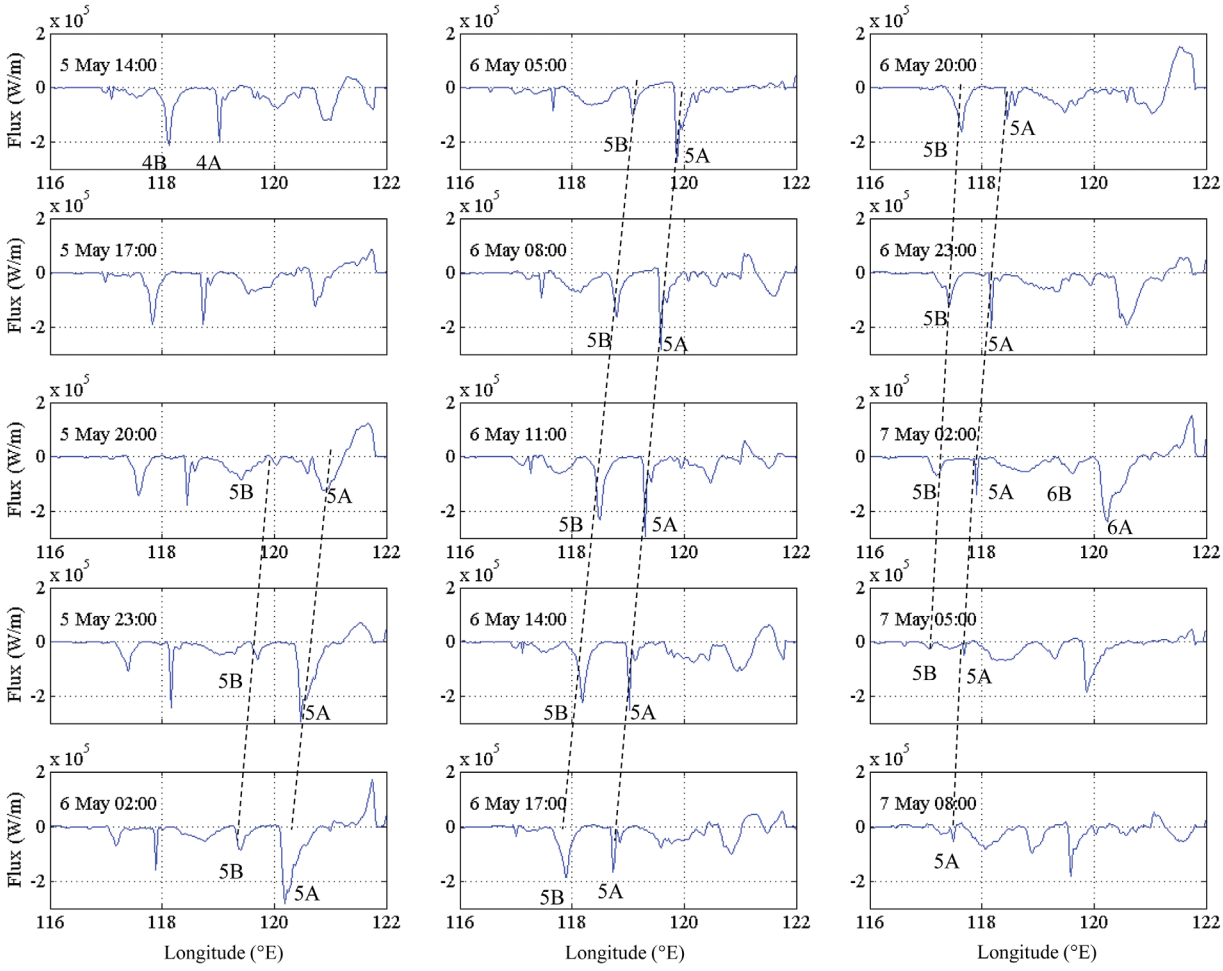


**Figure 7.** Depth-integrated energy flux as a function of longitude. The first plot is at 14:00 on 5 May 2007. Each panel has a 3 h lag from the previous one. ISWs are labeled as in Figure 6.

15B by 26 h, and wave 13B leads 15A by 47 h with a wave trough between 13B and 15A. The trough may be labeled as 14B for a wave generated on the western ridge after 13B. Note that two semidiurnal peaks are present in the eastward tidal velocity on May 14 (Figure 3). Wave 14B could also be 14A generated on the eastern ridge by the semidiurnal peak 12 h earlier, but the precise label is not important. Figure 6 shows that two waves arrive each day from each of the two wave sequences 12A–13A–15B–16B and 13B–14B–15A–16A. The pattern clearly indicates exchange of the arrival times of a B-wave and an A-wave. The transition from one wave type to the other was noted by *Vlasenko et al*. [2012] and will be discussed in more detail in section 3.4.

### 3.3. Wave Propagation

[24] Internal wave propagation can be observed in the plot of depth-integrated energy flux as a function of longitude from 5 to 7 May (Figure 7). From Figure 6, negative peaks in Figure 7 are identified and labeled. At 14:00 h on 5 May, waves 4B and 4A are located between 118°E and 119.3°E with 4A being narrower than 4B. The two waves propagate westward to 117°E, where 4B and 4A have dissipated by 05:00 and 20:00, respectively, on 6 May. Waves 5B and 5A cannot be identified until 20:00 on 5 May. Wave 5A intensifies quickly to form a narrow peak at 14:00 on 6 May. It decays afterward but can be traced to 117.5°E at 8:00 h on 7 May. Wave 5B forms a broader peak than wave 5A. It strengthens until 14:00 on 6 May and is identifiable at 117°E at 5:00 on 7 May. Narrower A-wave and broader B-waves were observed by *Ramp et al*. [2004] and *Alford et al*. [2010].

[25] Wave propagation in the vertical cross section during the same period is shown in the contour plot of the eastward baroclinic velocity (Figure 8). An ISW is represented by a patch of negative baroclinic velocity at the location of large integrated energy flux in Figure 7. On 5 May, the eastward tidal current is a maximum at 8:00 h and decreases to zero 5 h later (Figure 3). At 14:00 h, 6 h after the peak eastward flow, 5B appears as a wave beam originating from the east slope of the western ridge. Wave 5B is vague in the next three panels as it propagates along a wave beam, but appears as a distinct surface patch at 119.4°E at 2:00 h on 6 May. It reaches the shelf edge at 2:00 h on 7 May. From the eastern ridge, a patch of negative velocity (wave 5A) appears in shallow depths on the west slope. It encounters a wave beam from the western ridge in the next panel and continues propagating to

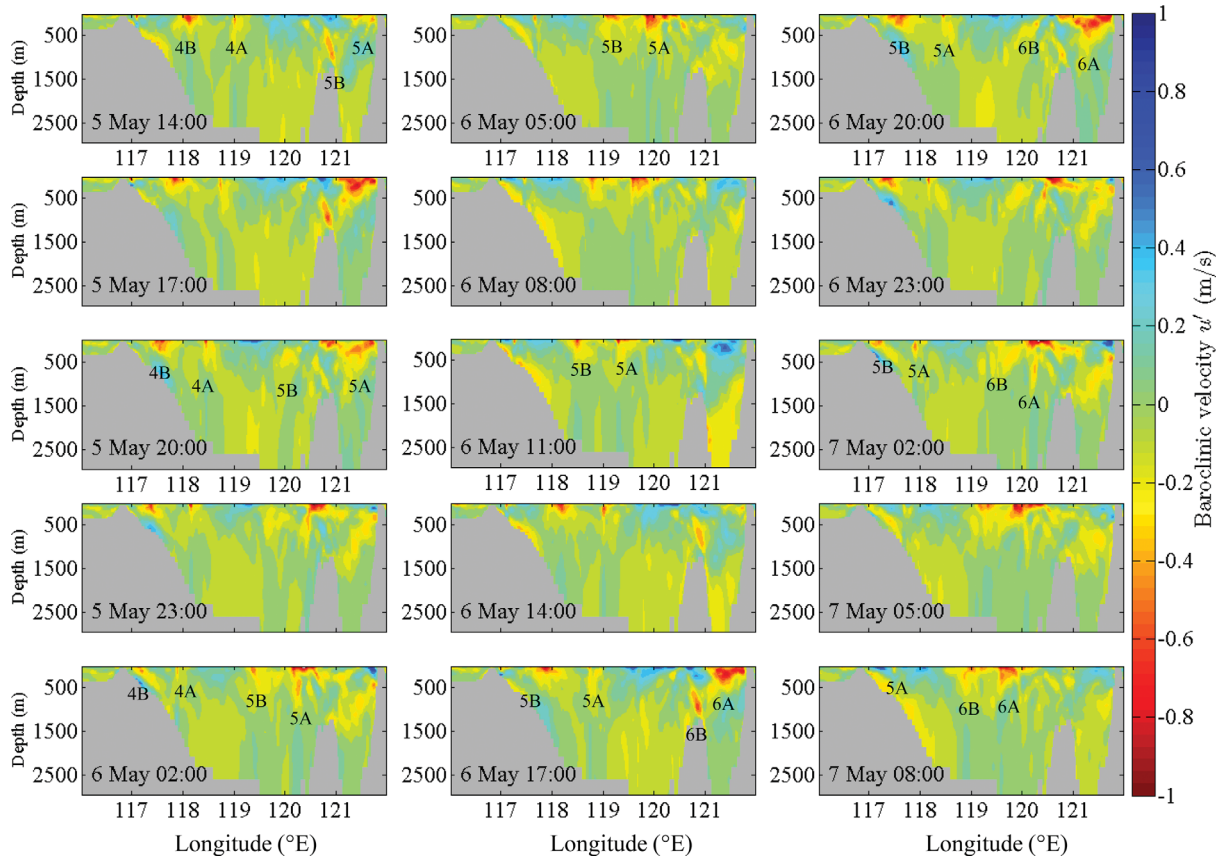


**Figure 8.** Baroclinic velocity in the vertical section of 20.81°N. The time is the same as in Figure 7. The contour interval is 0.1 m/s.

120.9°E at 20:00 h on 5 May, as in the energy flux plot. Wave 5A then propagates westward behind 5B and dissipates when approaching the shelf edge.

[26] Figure 8 shows that 5A starts in a nearly horizontal wave beam and becomes a mode-1 wave after passing the western ridge. The wave beam of 5B is more vertical and originates from the east side of the western ridge. The mode-1 structure of 5B appears west of 120°E. Waves 5B and 5A are behind the wave pair 4B and 4A in the first four panels and are ahead of 6B and 6A in the last four panels. Note that 5A is closely behind 5B without a region of positive surface flow in between, supporting the argument in section 3.1 that B-waves are not generated on the eastern ridge. Again, the wave propagation sequence mentioned in observation [e.g., *Alford et al*., 2010] is preserved.

### 3.4. Time of Arrival

[27] It has been observed that an A-wave arrives at a fixed longitude nearly at the same time each day and the arrival of a B-wave is delayed by approximately 1 h each day [*Ramp et al*., 2004]. Figure 9 shows the hour of arrival at 119°E each day in May for waves 2A–24A and 2B–24B. The longitude 119°E is used because the signal-to-noise ratio for both A- and B-waves is higher than that at 119.5°E. For waves generated on and before 6 May, time of the peak spring tide (Figure 3), waves 2A–6A arrive at the same time each day while waves 2B–6B show a 1 h delay in the arrival time as in observations. From 6 to 11 May, both A-waves (7A–11A) and B-waves (6B–11B) have a 1 h delay in arrival each day. When a semidiurnal tidal component appears after May 11 (Figure 3), B-waves (12B–14B) arrive at the same time each day, and A-waves (12A–13A) maintain a 1 h delay in their daily arrivals. After the exchange in the arrival times of a B-wave and an A-wave, A-waves (15A–20A) again arrive at the same time

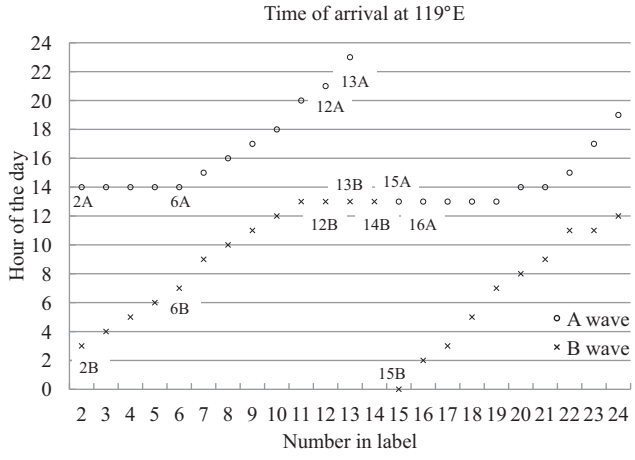


**Figure 9.** The daily arrival times of A- and B-waves at 119°E in May 2007. The horizontal axis is the date in the wave label. The vertical axis is the hour of the day from 0:00 to 24:00.

each day while B-waves (15B–20B) show a 1 h delay in the arrival time.

[28] The wave sequences 13B–14B–15A–16A and 12A–13A–15B–16B are consistent with those obtained in section 3.2. Figure 9 shows that the switch in arrival times maintains the order that an A-wave always arrives behind a B-wave in less than 12 h. At the diurnal period, the phase lag is less than 180°, consistent with the observation that A-waves follow B-waves closely. The result confirms the wave arrival sequence used in sections 3.1 and 3.2.

[29] Figure 9 shows that A-waves have the same daily arrival time when they are stronger during the first half of the spring tide. B-waves have a 1 h delay in daily arrival at all times except when they are weaker during the neap tide. These are likely the reason why the same arrival time for A-waves and 1 h delay for B-waves were noted in observation. *Vlasenko et al*. [2012] also found changes in the arrival time and role switching for A-waves and B-waves in their analysis. Using the terminology introduced by *Ramp et al*. [2004], they classified a multiple-wave packet as an A-wave and a single-wave packet as a B-wave. In their Figure 8, two A-waves or two B-waves could be present in a day with transitions from a B-wave to an A-wave and to a B-wave again in 4 days. Their interpretation is inconsistent with the observation of *Alford et al*. [2010]. Figure 9 shows that the definitions for A-waves and B-waves based on generation give a consistent description of wave generation and propagation.

### 3.5. Speed of Propagation

[30] Waves generated during two fortnightly cycles between 25 April and 25 May are used to calculate the speed of wave propagation. The region between 121.5°E and 117°E is divided into 0.5° intervals. In each interval, the speed of individual waves is obtained from the difference in arrival time and averaged for A-waves and B-waves separately. The speed of A-waves is 3 m/s at 121.25°E before reaching the western ridge (Figure 10a). It increases to a peak value of 3.6 m/s at 120.75°E and decreases to a nearly constant speed around 3 m/s in the deep basin. It further decreases to 2.2 m/s at 117.75°E. The speed of B-waves is 2.4 m/s initially and increases to a peak value of 3.2 m/s at120.25°E (Figure 10b). It is nearly constant at 3 m/s in the deep basin and decreases to 2.1 m/s on the continental slope. Figure 10 shows a slower speed of propagation at generation and an increase in speed after generation for both wave types. The initial speed of A-waves seems to be higher than that of B-waves. Both waves propagate at nearly the same speed in the deep basin and slow down when approaching the continental slope although A-waves slow down earlier than B-waves. Speeds for both wave types are higher than the phase speed of linear internal waves. The speed agrees with the observations in Figure 5 of *Alford et al*. [2010].

[31] Westward propagating internal waves are released not at the peak eastward tidal current but at the reversal of the tidal current from eastward to westward [*Shaw et al*., 2009; *Buijsman et al*., 2010]. The speeds in Table 1 are estimated from the difference in wave arrival time and time of the peak eastward tidal current. If the 3 h lag between the peak eastward tidal current and the slack tide is considered, the speeds for scenario 2 in Table 1 will be 2.7–3.0 m/s and 2.8–3.3 m/s for B-waves and A-waves, respectively. These values agree well with the speeds for both types of waves east of 119.5°E in Figure 10. The speed calculation again validates the wave generation scheme used in this study.

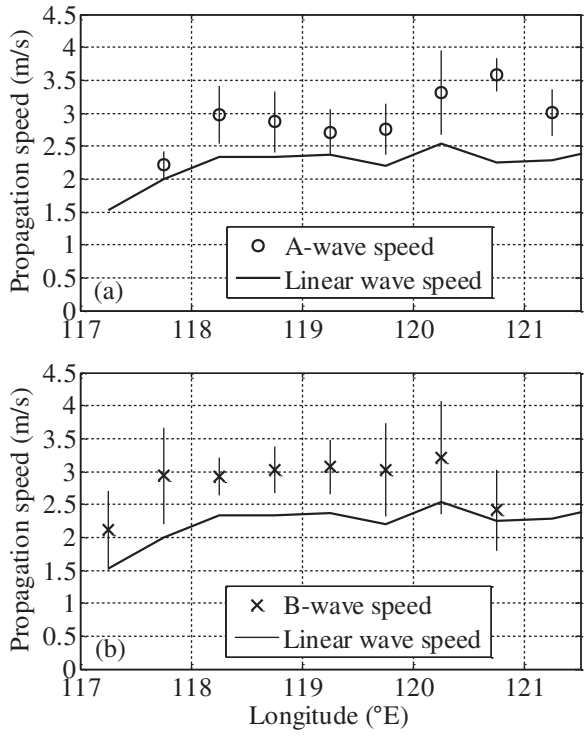


**Figure 10.** The average speed of propagation for 30 A-waves and 29 B-waves as a function of longitude. The error bar represents one standard deviation. The phase speed of the linear internal wave is shown.

## 4. Discussion

[32] Mode-1 and mode-2 internal solitary waves have prominent signatures in the upper ocean and can be detected in satellite imagery and in mooring observations of temperature and baroclinic velocity [*Ramp et al*., 2004; *Yang et al*., 2004]. These observations have provided a comprehensive view of internal wave propagation in the deep basin of the northern South China Sea. However, it is difficult to describe the wave field in the generation region from mooring observations because of the three-dimensional propagation of internal wave beams and the superposition of eastward and westward propagating waves. The internal wave field in the Luzon Strait is also not reproduced adequately in real time in nonhydrostatic simulation that uses either the same density profile over the entire domain or two-dimensional topography [e.g., *Zhang et al*., 2011; *Vlasenko et al*., 2012]. Using data from a three-dimensional nowcast simulation, this study calculates the barotropic velocity, the baroclinic velocity, and the depth-integrated energy flux in the Luzon Strait and the northern South China Sea in a 2 month period overlapping the observation of *Alford et al*. [2010]. The model is hydrostatic, producing less sharp fronts of internal solitary waves than in a nonhydrostatic model. Nevertheless, the location

of internal solitary waves is adequately described in plots of the depth-integrated zonal energy flux.

[33] To date the most comprehensive observation of internal waves in the South China Sea is that of *Alford et al*. [2010]. Fourteen ISWs were documented during the period 26 April to 7 May 2007, using data from 10 moorings spanning from 116°E to 122°E at approximately 21°N. The result in section 3 compares favorably with the observation of *Alford et al*. [2010]; all waves in Figure 5 of *Alford et al*. [2010] have been identified in Figure 6. Besides the gross comparison, several features also agree. The sequence of wave arrival is consistent with the observed pattern that A-waves follow B-waves more closely than vice versa. The speed in Figure 10 also agrees with the speed observed between 117°E and 120°E in Figure 5 of *Alford et al*. [2010]. The result shows that the depth-integrated energy flux provides adequate longitude-time information for extrapolation to the starting time and longitude at generation.

[34] Based on the arrival times in the deep basin, *Alford et al*. [2010] rejected the idea that wave generation at the eastern ridge is by the westward tidal flow [*Zhao and Alford*, 2006]. Instead, they suggested that wave generation is shortly after the maximum eastward tidal currents. This generation time is consistent with the timing inferred in section 3.1. However, *Alford et al*. [2010] could not explain the asymmetry in the arrival times of A- and B-waves with both waves generated at the eastern ridge. The present study resolves the problem in arrival time by assuming that A- and B-waves are generated at different ridges by the same peak ebb tide. Being generated closer to the observation site, B-waves arrive at a site west of the western ridge before A-waves.

[35] Using a nonhydrostatic model, *Zhang et al*. [2011] analyzed the internal wave field in the northern South China Sea during June–July 2005. They found that A-waves consistently line up with peak eastward (ebb) barotropic tidal currents as in this study. However, they associate B-waves to peak westward (flood) currents. The present study argues that this hypothesis of wave generation violates the observed sequence of wave arrival. In *Zhang et al*. [2011], a single observed density profile in the South China Sea is used over the entire domain. Generation of the internal wave is strongly affected by stratification [e.g., *Qian et al*., 2010]. Without using the Kuroshio stratification in the Luzon Strait, the internal wave beam may not be adequately represented in their study.

[36] That the B-wave and A-wave are generated by the eastward tidal current at the western ridge and eastern ridge, respectively, is supported by theory. In the internal tide release mechanism of *Buijsman et al*. [2010], isotherms are lifted by the eastward tidal currents to form an elevation wave on the west side of a ridge. When the tidal current starts to turn westward, the wave crest is released, and internal solitary waves form on the back slope of the elevation waves. The eastern ridge is above the thermocline, allowing the strong eastward tidal current to lift the isotherm higher on the west side of the eastern ridge. An example is wave 5A in Figure 8. Thus, generation of A-waves at the eastern ridge by eastward tidal currents could be explained by the internal tide release mechanism. This mechanism cannot be applied on the western ridge, which is lower than the thermocline. It is possible that B-waves are generated by the lee-wave mechanism of *Maxworthy* [1979]. In this mechanism, a depression forms on the right side of the ridge during ebb flow. When the eastward current slackens, this lee depression moved westward over the ridge and evolved into westward propagating solitary waves. In Figure 8, wave 5B appears in a wave beam on the right side of the western ridge 1 h after the sack water and is in agreement with the lee-wave mechanism.

## 5. Conclusion

[37] ISWs in the South China Sea have been classified as A- and B-waves. Previous observations have described differences in the daily arrival time, intensity of energy flux, width of the wave crest on the surface, phase speed, etc. However, the sources of these two types of waves have not been resolved in mooring observations and numerical models. In this study, the surface baroclinic velocity and internal wave energy flux integrated through the water column are used to track propagation of internal waves. With extensive spatial coverage of the two variables in the numerical model, trajectories of internal waves along 20.81°N during April–May 2007 are derived. The internal wave field of *Alford et al*. [2010] is reproduced in the Luzon Strait and the northern South China Sea. It is concluded that A- and B-waves are generated on the eastern and western ridges, respectively, by the eastward (ebb) tidal current and released westward when the tidal current turns westward.

[38] The above scenario is supported by the sequence of wave arrival at locations west of the generation sites. Waves generated at the two ridges by the eastward tidal current arrive in the deep basin in a particular order. A wave crest with positive surface velocity arrives first, followed by a B-wave and then an A-wave in less than 12 h. This sequence is shown in Figure 4 during the spring tide when there is only one large diurnal peak in the eastward tidal current. During the neap tide, when the maximum eastward tidal velocity shows a time shift of 12 h, the B-wave and the A-wave switch their daily arrival times to maintain the arrival sequence of an A-wave after a B-wave. This specific order, confirmed by earlier observations, plays an important role in the propagation of internal solitary waves in the South China Sea.

[39] Internal waves arriving at a mooring location in the South China Sea at the same time each day are B-waves during neap tide and A-waves during the first half of the spring tide. At other times, both A-waves and B-waves have a 1 h delay each day. The speed of wave propagation calculated from the wave trajectory agrees with the scenario that waves are generated at two ridges by the same eastward tidal current. The result provides a consistent description of the internal wave field in both the generation and propagation regions of the South China Sea.

[40] **Acknowledgments.** This work was supported by the Office of Naval Research grant N00014-10-1-0470 to North Carolina State University and N00014-05WX-2-0647 to D. S. K. We thank the helpful comments from two reviewers.

## References

Alford, M. H., R.-C. Lien, H. Simmons, J. Klymak, S. Ramp, Y.-J. Yang, D. Tang, and M.-H. Chang (2010), Speed and evolution of nonlinear

internal waves transiting the South China Sea, *J. Phys. Oceanogr.*, *40*, 1338–1355, doi:10.1175/2010JPO4388.1.

Alford, M. H., et al. (2011), Energy flux and dissipation in Luzon Strait: Two tales of two ridges, *J. Phys. Oceanogr.*, *41*, 2211–2222, doi:10.1175/JPO-D-11–073.1.

Apel, J. R., H. M. Byrne, J. R. Proni, and R. L. Charnell (1975), Observations of oceanic internal and surface-waves from earth resources technology satellite, *J. Geophys. Res.*, *80*(6), 865–881, doi:10.1029/JC080i006p00865.

Bloomfield, P. (2000), *Fourier Analysis of Time Series: An Introduction*, 2nd ed., John Wiley, New York.

Buijsman, M. C., Y. Kanarska, and J. C. McWilliams (2010), On the generation and evolution of nonlinear internal waves in the South China Sea, *J. Geophys. Res.*, *115*, C02012, doi:10.1029/2009JC005275.

Chao, S.-Y., D. Ko, R.-C. Lien, and P.-T. Shaw (2007), Assessing the west ridge of Luzon Strait as an internal wave mediator, *J. Oceanogr.*, *63*(6), 897–911, doi:10.1007/s10872-007-0076-8.

Egbert, G. D., and S. Y. Erofeeva (2002), Efficient inverse modeling of barotropic ocean tides, *J. Atmos. Ocean. Technol.*, *19*, 183–204, doi:10.1175/1520-0426(2002)019<0183:EIMOBO>2.0.CO;2.

Finnigan, T. D., D. S. Luther, and R. Lukas (2002), Observations of enhanced diapycnal mixing near the Hawaiian Ridge, *J. Phys. Oceanogr.*, *32*, 2988–3002, doi:10.1175/1520-0485(2002)032<2988:OOEDMN>2.0.CO;2.

Holligan, P. M., R. D. Pingree, and G. T. Mardell (1985), Oceanic solitons, nutrient pulses and phytoplankton growth, *Nature*, *314*, 348–350, doi:10.1038/314348a0.

Kaartvedt, S., T. A. Klevjer, and D. L. Aksnes (2012), Internal wave-mediated shading causes frequent vertical migrations in fishes, *Mar. Ecol. Prog. Ser.*, *452*, 1–10, doi:10.3354/meps09688.

Klemas, V. (2012), Remote sensing of ocean internal waves: An overview, *J. Coastal Res.*, *28*(3), 540–546, doi:10.2112/JCOASTRES-D-11–00156.1.

Klymak, J. M., R. Pinkel, C.-T. Liu, A. K. Liu, and L. David (2006), Prototypical solitons in the South China Sea, *Geophys. Res. Lett.*, *33*, L11607, doi:10.1029/2006GL025932.

Ko, D. S., P. J. Martin, C. D. Rowley, and R. H. Preller (2008), A real-time coastal ocean prediction experiment for MREA04, *J. Mar. Syst.*, *69*, 17–28, doi:10.1016/j.jmarsys.2007.02.022.

Ko, D. S., S.-Y. Chao, P. Huang, and S. F. Lin (2009), Anomalous upwelling in Nan Wan: July 2008, *Terr. Atmos. Ocean. Sci.*, *20*, 839–852, doi:10.3319/TAO.2008.11.25.01(Oc).

Lee, C.-Y., and R. C. Beardsley (1974), Generation of long nonlinear internal waves in a weakly stratified shear flow, *J. Geophys. Res.*, *79*(3), 453–462, doi:10.1029/JC079i003p00453.

Lien, R.-C., T. Y. Tang, M. H. Chang, and E. A. D'Asaro (2005), Energy of nonlinear internal waves in the South China Sea, *Geophys. Res. Lett.*, *32*, L05615, doi:10.1029/2004GL022012.

Maxworthy, T. (1979), Note on the internal solitary waves produced by tidal flow over a 3-dimensional ridge, *J. Geophys. Res.*, *84*, 338–346, doi:10.1029/JC084iC01p00338.

Moore, S. E., and R.-C. Lien (2007), Pilot whales follow internal solitary waves in the South China Sea, *Mar. Mamm. Sci.*, *23*, 193–196, doi:10.1111/j.1748–7692.2006.00086.x.

Nash, J. D., M. H. Alford., and E. Kunze (2005), Estimating internal wave energy fluxes in the ocean, *J. Atmos. Ocean. Technol.*, *22*, 1551–1570, doi:10.1175/JTECH1784.1.

Osborne, A. R., and T. L. Burch (1980), Internal solitons in the Andaman Sea, *Science*, *208*(4443), 451–460, doi:10.1126/science.208.4443.451.

Pomar, L., M. Morsilli, P. Hallock, and B. Bádenas (2012), Internal waves, an under-explored source of turbulence events in the sedimentary record, *Earth Sci. Rev.*, *111*(2), 56–81, doi:10.1016/j.earscirev.2011.12.005.

Qian, H., P.-T. Shaw, and D. S. Ko (2010), Generation of internal waves by barotropic tidal flow over a steep ridge, *Deep Sea Res., Part I*, *57*, 1521–1531, doi:10.1016/j.dsr.2010.09.001.

Quaresma, L. S., J. Vitorino, A. Oliveira, and J. da Silva (2007), Evidence of sediment resuspension by nonlinear internal waves on the western Portuguese mid-shelf, *Mar. Geol.*, *246*(2–4), 123–143, doi:10.1016/j.margeo.2007.04.019.

Ramp, S. R., T. Y. Tang, T. F. Duda, J. F. Lynch, A. K. Liu, C. S. Chiu, F. L. Bahr, H.-R. Kim, and Y.-J. Yang (2004), Internal solitons in the northeastern South China Sea—Part I: Sources and deep water propagation, *IEEE J. Oceanic Eng.*, *29*(4), 1157–1181, doi:10.1109/JOE.840839.

Shaw, P.-T., D. S. Ko, and S.-Y. Chao (2009), Internal solitary waves induced by flow over a ridge: With applications to the northern South China Sea, *J. Geophys. Res.*, *114*, C02019, doi:10.1029/2008JC005007.

Vlasenko, V., C. Guo, and N. Stashchuk (2012), On the mechanism of A-type and B-type internal solitary wave generation in the northern South China Sea, *Deep Sea Res., Part I*, *69*, 100–112, doi:10.1016/j.dsr.2012.07.004.

Williams, K. L., F. S. Henyey, D. Rouseff, S. A. Reynolds, and T. E. Ewart (2001), Internal wave effects on high-frequency acoustic propagation to horizontal arrays-experiment and implications to imaging, *IEEE J. Oceanic Eng.*, *26*(1), 102–112, doi:10.1109/48.917939.

Yang, Y.-J., T. Y. Tang, M. H. Chang, A. K. Liu, M.-K. Hsu, and S. R. Ramp (2004), Solitons northeast of Tung-Sha Island during the ASIAEX pilot studies, *IEEE J. Oceanic Eng.*, *29*(4), 1182–1199, doi:10.1109/JOE.2004.841424.

Zhang, Z., O. B. Fringer, and S. R. Ramp (2011), Three-dimensional, nonhydrostatic numerical simulation of nonlinear internal wave generation and propagation in the South China Sea, *J. Geophys. Res.*, *116*, C05022, doi:10.1029/2010JC006424.

Zhao, Z., and M. H. Alford (2006), Source and propagation of internal solitary waves in the northeastern South China Sea, *J. Geophys. Res.*, *111*, C11012, doi:10.1029/2006JC003644.

Zhao, Z., V. Klemas, Q. Zheng, and X.-H. Yan (2004), Remote sensing evidence for baroclinic tide origin of internal solitary waves in the northeastern South China Sea, *Geophys. Res. Lett.*, *31*, L06302, doi:10.1029/2003GL019077.

Zheng, Q., R. D. Susanto, C.-R. Ho, Y. T. Song, and Q. Xu (2007), Statistical and dynamical analyses of generation mechanisms of solitary internal waves in the northern South China Sea, *J. Geophys. Res.*, *112*, C03021, doi:10.1029/2006JC003551.